Channel opening and gating mechanism in AMPA-subtype glutamate receptors

Edward C. Twomey[1,2], **Maria V. Yelshanskaya**[1], **Robert A. Grassucci**[1,4], **Joachim Frank**[1,3,4], and **Alexander I. Sobolevsky**[1,*]

[1]Department of Biochemistry and Molecular Biophysics, Columbia University, 650 West 168th Street, New York, NY 10032

[2]Integrated Program in Cellular, Molecular, and Biomedical Studies, Columbia University, 650 West 168th Street, New York, NY 10032

[3]Department of Biological Sciences, Columbia University, 650 West 168th Street, New York, NY 10032

[4]Howard Hughes Medical Institute, 650 West 168th Street, New York, NY 10032

Summary

AMPA-subtype ionotropic glutamate receptors mediate fast excitatory neurotransmission throughout the central nervous system. Gated by the neurotransmitter glutamate, AMPA receptors are critical for synaptic strength and dysregulation of AMPA receptor-mediated signaling is linked to numerous neurological diseases. Here, we use cryo-electron microscopy to solve the structures of AMPA receptor-auxiliary subunit complexes in the apo, antagonist and agonist-bound states and elucidate the iris-like mechanism of ion channel opening. The ion channel selectivity filter is formed by the extended portions of the re-entrant M2 loops, while the helical portions of M2 contribute to extensive hydrophobic interfaces between AMPA receptor subunits in the ion channel. We show how the permeation pathway changes upon channel opening and identify conformational changes throughout the entire AMPA receptor that accompany activation and desensitization. Our findings provide a framework for understanding gating across the family of ionotropic glutamate receptors and the role of AMPA receptors in excitatory neurotransmission.

*Correspondence: as4005@cumc.columbia.edu.
Correspondence and requests for materials should be addressed to A.I.S. (as4005@cumc.columbia.edu).

Supplementary Information is linked to the online version of the paper.

The authors declare no competing financial interests.

Readers are welcome to comment on the online version of the paper.

Excitatory neurotransmission is tightly governed by the α-amino-3-hydroxy-5-methyl-4-isoxazolepropionic (AMPA) subtype of the ionotropic glutamate receptors (iGluRs)[1,2]. Gated by the neurotransmitter glutamate, AMPA receptors (AMPARs) activate on a sub-millisecond timescale and rapidly depolarize the post-synaptic membrane. AMPAR-mediated neuronal signaling has profound effects on synaptic strength, and many neurological diseases have been directly linked to changes in AMPAR synaptic signaling[3–5].

AMPARs are tetrameric, two-fold symmetric membrane proteins with a three-layer, "Y"-shaped architecture[6,7]. Extracellularly, the amino-terminal domains (ATDs) form the top of the "Y." Below the ATDs are the ligand binding domains (LBDs) that bind the neurotransmitter glutamate. Two polypeptide stretches (S1 and S2) make up each of the four AMPAR subunit LBDs, which are tethered to the transmembrane domain (TMD) at the base of the "Y" by flexible linkers. The nearly four-fold symmetric TMD is made up of three membrane-spanning helices (M1, M3 and M4) and a re-entrant pore loop (M2) between helices M1 and M3. The cation-selective ion channel is lined by the M3 helices with their bundle crossing forming a tight gate to regulate permeation.

Since the first, closed-state intact AMPAR structure[8], many studies have pursued different receptor conformations using both X-ray crystallography[9–12] and cryo-electron microscopy (cryo-EM)[13–17]. However, the structure of the ion channel is yet to be resolved to high-resolution, and the open-state of the receptor has yet to be seen. This is a fundamental barrier to understanding AMPAR biology and structurally-informed design of therapeutics targeting AMPARs in neuropathological conditions. Here, we use cryo-EM to solve the structure of an AMPAR ion channel to high resolution and resolve opening of the AMPAR ion channel in response to binding of glutamate.

Ion Channel Structure

We used cryo-EM to analyze the structure of the homomeric GluA2 flip splice variant AMPAR in complex with the auxiliary subunit germline-specific gene 1-like (GSG1L), which we surmised would stabilize the closed-state structure of the ion channel as it lowers the ion channel open probability compared to the transmembrane AMPAR regulatory protein (TARP)-γ2 or stargazin (STZ)[15,16]. Indeed, using a covalent fusion construct (Methods) between truncated forms of GluA2 and GSG1L, we solved structures of the digitonin-solubilized receptor complex bound to the antagonist ZK200775 (ZK) in two states, termed GluA2-GSG1L$_{ZK-1}$ (4.6 Å) and GluA2-GSG1L$_{ZK-2}$ (4.4 Å) (Extended Data Table 1; Extended Data Fig. 1), with local qualities of the maps showing higher resolution details in the ion channel pore (Extended Data Fig. 2).

The GluA2-GSG1L$_{ZK-1}$ complex has a typical Y-shaped GluA2 tetramer in the center (Fig. 1a), with two GSG1L subunits assembling between protomers A/B and C/D on the periphery of the GluA2 TMD (Fig. 1b). The GluA2 TMD is completely resolved and allows building of the entire ion channel pore-forming region (Fig. 1c–d). The M3 bundle crossing, formed by T617, A621, T625 and M629, occludes cation permeation, as previously observed in the original GluA2 crystal structure[8]. Below T617, the M3 bundle crossing opens up into a hydrophobic cavity in the middle of the channel pore. Below this cavity is a second

constriction formed by the extended regions of the M2 re-entrant loops. Similar to other tetrameric ion channels, this constriction might serve as a lower gate of the channel as well as a selectivity filter[18–20]. At the re-entrant loop tip, the Q/R-site glutamines (Q586) protrude towards the center of the ion channel pore, occluding the permeation pathway and forming a lower gate. Their location is consistent with the observation that channels composed of edited GluA2 subunits (Q586R) have reduced Ca^{2+} permeation and polyamine block, likely due to electrostatic repulsion[21,22]. The pore loop, under the Q/R-site, appears to be more flexible in our closed-state structures, compared to the rest of the channel, but we expect it to become more ordered upon channel opening to form a selectivity filter along the permeation pathway.

The α-helical portion of M2 is largely hydrophobic (Fig. 1c) and contributes to cross-subunit interfaces within the TMD (Extended Data Fig. 3b). These hydrophobic interactions involve L540 and Y533 from M1, as well as W605 and F608 from the neighboring M3, each from the same subunit as the M2, and W606 and I600 from M3 of the adjacent subunit. The M2 helix contributes to these hydrophobic interfaces through L577, W578, L581 and F584. For a helix that has often evaded structural studies, the M2 helix has quite an extensive network of hydrophobic interactions.

The second closed state structure, GluA2-GSG1L$_{ZK-2}$, has the same ion channel architecture as in GluA2-GSG1L$_{ZK-1}$, though with higher resolution details throughout the TMD (Extended Data Fig. 2). While the TMD structure is the same, the ECD in GluA2-GSG1L$_{ZK-2}$ is astonishingly different, being shorter by 6 Å (Extended Data Fig. 4). The ATD rotates 19° as a rigid body around the overall two-fold axis of symmetry (Extended Data Fig. 4c–d), and the LBD dimers rotate by 4°, creating a separation between the proximal subunits A and C (Extended Data Fig. 4e–f). An elongated density at the ATD-LBD interfaces inside subunits A and C perfectly matches a digitonin molecule (Extended Data Fig. 4b, inset). Thus, digitonin binding might help to trap GluA2 in a distinct closed state conformation. We hypothesize that the ATD-LBD interface represents a novel binding site for hydrophobic molecules with a possible therapeutic significance and may bind fatty acids that have recently been identified as novel AMPAR noncompetitive inhibitors[23,24].

Cryo-EM of activated GluA2-STZ complex

To understand how the native neurotransmitter glutamate (Glu) activates and opens the AMPAR ion channel, we used a fusion construct between GluA2 and STZ (Methods) that promotes GluA2-STZ complex formation and expression while maintaining its functional properties. In contrast to GSG1L, which stabilizes the AMPAR inactive states, STZ favors the open state[25–27], as signified by increased steady-state current in response to Glu application in whole-cell patch-clamp recordings (Fig. 2a). Additional stabilization of the open state is provided by the positive allosteric modulator cyclothiazide (CTZ)[28], which makes AMPAR responses non-desensitizing (Fig. 2a).

We solved a cryo-EM structure of the GluA2-STZ complex in the presence of Glu and CTZ to 4.2 Å resolution (Extended Data Fig. 1), with two-dimensional class averages showing the secondary structure features and diverse orientations (Fig. 2b). The reconstruction (Fig. 2c)

shows the entire GluA2-STZ complex in the agonist-bound state, with high-resolution features in the GluA2 TMD core (Extended Data Figs 2n and 2o) but lower local resolution for STZ. To achieve unambiguous side chain definition in the TMD, we performed directed refinement (Fig. 2c) that resulted in a 4.0 Å cryo-EM reconstruction (Fig. 2d) and distinct side chain densities (Extended Data Fig. 5e). The TMD cryo-EM map shows clear differences in the central pore (Fig. 2e) compared to the closed-state GluA2-GSG1L complex (Fig. 1b) and four STZ molecules bound. Also, glutamate and CTZ are easily discernible in the cryo-EM density (Extended Data Figs 5a and 5d), suggesting that we trapped the complex in an activated state.

The original, closed-state cryo-EM structures of the GluA2-STZ complex suggested that acidic residues in the STZ β4-TM2 loop mediate electrostatic interactions with positively charged residues in the lower GluA2 LBD and S1-pre-M1 linker to enhance receptor activation[17,29]. In our active state cryo-EM reconstruction, this region of STZ appears to be disordered. However, based on well-defined adjacent regions of STZ (Extended Data Fig. 5e), the same acidic residues are juxtaposed to the GluA2 basic patch. Perhaps rather than directly interacting in the activated state, the β4-TM2 loop plays an important role in the structural transitions necessary for receptor activation.

Our density, and the corresponding GluA2-STZ$_{Glu+CTZ}$ model (Fig. 3, Methods) show four STZ molecules bound around the AMPAR core (Fig. 2e, Extended Data 6c). We used the same fusion design to solve the first structure of the GluA2-STZ complex in the closed state[15] but observed only one or two STZ molecules bound to the AMPAR core. Here we solubilized the complex in digitonin instead of dodecyl maltoside (DDM) detergent and observed maximum occupancy of STZ binding sites around the AMPAR core, similar to GluA2-STZ co-expression[17]. Accordingly, instead of the four-layer particle architecture in DDM[15], we now see a clearly discernible three-layer architecture in the two-dimensional (2D) class averages (Extended Data Fig. 6a). Interestingly, the GluA2-GSG1L complex in digitonin, which showed a four-layer architecture when solubilized in DDM[16], also showed the three-layer particle architecture (Extended Data Fig. 6b) but with only two, not four, molecules of GSG1L bound to GluA2 core (Fig. 1a, Extended Data Fig. 6d). As the nature of the fusion construct design does not preclude full occupancy of the auxiliary subunit binding sites, we hypothesize that STZ and GSG1L use different stoichiometries to assemble with AMPARs.

Open ion channel pore

As indicated by the markedly different architecture of the AMPAR core in GluA2-STZ$_{Glu+CTZ}$ compared to the closed state, the width of the TMD increases by 10 Å from 55 Å in the closed state structures to 65 Å in GluA2-STZ$_{Glu+CTZ}$, and the ion channel pore undergoes widening (cf. Figs. 1b and 3b). We probed the ion conduction pathway in GluA2-STZ$_{Glu+CTZ}$ (Fig. 4a) and found it much wider than in the closed state GluA2-GSG1L structures (Fig. 1d). Measurements of the pore radius (Fig. 4b) confirmed that in contrast to the pore-occluded conformations in the closed GluA2-GSG1L$_{ZK-1}$, GluA2-GSG1L$_{ZK-2}$ and desensitized GluA2-GSG1L$_{Quis}$[16] states, the GluA2-STZ$_{Glu+CTZ}$ pore is wide open for ion conductance. The distances between Cα's of diagonal Q586, T617 and A621 pairs increased

almost uniformly by about 3 Å in GluA2-STZ$_{Glu+CTZ}$ (Fig. 4b–c) signifying nearly 4-fold symmetric, iris-type opening of the main portion of the pore (Fig. 4d), reminiscent of other tetrameric ion channels[19,30,31]. In stark contrast, the distance between diagonal T625 pairs, which is similar for the A/C and B/D subunit pairs in the closed state (9.5 and 11 Å), increases to 16 Å for the A/C pair and to 32 Å for the B/D pair in GluA2-STZ$_{Glu+CTZ}$. This 6.5 Å versus 21 Å separation upon channel opening indicates that at the level of T625, the AMPAR pore loses its pseudo 4-fold symmetry and becomes two-fold symmetric, consistent with previous functional experiments[32]. We also compared our recent molecular dynamics (MD) model of the open state[33] and the GluA2-STZ$_{Glu+CTZ}$ structure. The narrowest portions of the pore in the MD model, estimated as Cα distances between the diagonal Q586 (9.6 Å) and T617 (12.6 Å) pairs, are narrower than the corresponding portions of the GluA2-STZ$_{Glu+CTZ}$ pore (10.2 Å and 14.1 Å, respectively). Yet, we clearly observed ion conducting events through our MD model[33], an observation strongly supporting the conducting conformation of the GluA2-STZ$_{Glu+CTZ}$ pore. In addition, a clear density in the center of the pore (Extended Data Figs 5b and 5c), likely representing a sodium ion, also suggests that the selectivity filter of the channel is indeed in a conducting state.

The selectivity filter located at and below the Q/R site (Fig. 4a–b), which is not visible in the closed-state, is clearly resolved in GluA2-STZ$_{Glu+CTZ}$ and is approximately four-fold symmetric, similar to K$^+$ channels[30,31]. Just below the Q/R site, the backbone carbonyls of Q587, G588 and C589 line the selectivity filter, while the side chains of Q587 and C589 point away from the central pore axis. At the bottom of the selectivity filter is D590 that creates a negative entry point into the cytoplasm from the channel pore, perhaps playing a role in cation versus anion selectivity of AMPAR channels.

Gating Mechanism

In order to understand the conformational changes that are associated with AMPAR gating we compared the open-state GluA2-STZ$_{Glu+CTZ}$ to the closed-state GluA2-GSG1L$_{ZK-1}$ and the desensitized-state GluA2-2xGSG1L$_{Quis}$ structures (Fig. 5, Video S1). Since gating starts with binding of glutamate to an unliganded AMPAR, we first wanted to see if GluA2-GSG1L$_{ZK-1}$ faithfully represents the resting, *apo* state of the receptor. We solved cryo-EM structures of the digitonin-solubilized GluA2-GSG1L complex in the absence of ligands, which, similarly to the ZK-bound structures, are represented by two different states. The *apo* state structures, GluA2-GSG1L$_{apo-1}$ and GluA2-GSG1L$_{apo-2}$, turned out to be very similar to GluA2-GSG1L$_{ZK-1}$ and GluA2-GSG1L$_{ZK-2}$ (Extended Data Figs 3 and 4), superposing on each other with the root mean square deviation (RMSD) of 0.526 Å and 0.701 Å, respectively. We therefore used the higher resolution GluA2-GSG1L$_{ZK-1}$ structure that is nearly identical to GluA2-GSG1L$_{apo-1}$ as a faithful representation of the closed resting state.

In the first approximation, activation, which includes ion channel opening, is represented by the GluA2-GSG1L$_{ZK-1}$ to GluA2-STZ$_{Glu+CTZ}$ transition. At the level of a single LBD, glutamate binding causes 26° LBD clamshell closure (Fig. 5a–d). Consistent with studies on isolated LBDs[34–36], this closure leaves the D1-D1 interface intact and leads to a 12 Å separation of the D2 lobes (Fig. 5e). The D2 separation results in widening of the LBD tetramer and expansion of the LBD gating ring in the middle of the LBD layer (Fig. 5g–h

and Extended Data Fig. 7g–h), which translates to pore opening by the LBD-TMD linkers (Fig. 5j–k).

We monitored conformational rearrangements in the S1-M1, M3-S2 and S2-M4 linkers by measuring distances between Cα's of the diagonal K505, S635 and G771 pairs. The M3-S2 linker in subunits B and D plays the central role in transmitting conformational changes in LBDs to opening of the ion channel, as signified by an 11 Å increase in S635 separation and a distinct kink in the M3 helix at A618 (Fig. 5j–k and Extended Data Fig. 5e), which turns the upper gate at the bundle crossing away from the central pore axis. The M3 helices in subunits A and C unwind and become one helical turn shorter, but the S635 separation in subunits A and C decreases by 1 Å, suggesting a weaker role in gating of the corresponding linkers. The S1-M1 linkers in subunits B and D make much more significant contribution to channel opening than the S1-M1 linkers in subunits A and C, with separation between K505 increasing by 13 and 5 Å, respectively. Unexpected changes were observed in the S2-M4 linkers in subunits A and C, which included complete unwinding of the pre-M4 helices (Fig. 5j–k) and stretching these linkers towards the center of the ion channel pore, while reducing the distance between G771 by 5 Å. These changes are in stark contrast to the S2-M4 linkers in subunits B and D, which maintain their relative positioning. The unprecedented conformational changes in the subunits A/C S2-M4 linkers that occur during channel opening support the importance of the M4 segments for iGluR function[37–39] and suggest a possible contribution of these linkers to the open pore extracellular vestibule.

We next mapped the changes between GluA2-STZ$_{Glu+CTZ}$ and GluA2-2xGSG1L$_{Quis}$[16] to assess conformational rearrangements during desensitization. Upon desensitization, individual LBDs maintain their closed clamshell conformation (Fig. 5a–d), while the LBD dimers undergo drastic rearrangements (Fig. 5f), signified by rupture of the D1-D1 interface (reduction in the S741 distance by 9 Å) allowing D2 lobes to come closer together (by 15 Å, measured as a change in the S635 distance) and permit channel closure. Rupture of the D1-D1 interface parallels loss of two-fold symmetry by individual LBD dimers, with 14° rotation of the A/C LBDs away from their B/D dimer partners and a more 4-fold symmetric LBD tetramer arrangement[16] signified by appearance of a cleft between local LBD dimers (Fig. 5i). Correspondingly, the D2 attachments to the LBD-TMD linkers in this new LBD tetramer arrangement acquire positions similar to the closed state, compressing the expanded open-state LBD gating ring (Fig. 5g–i). This results in the LBD-TMD linkers (Fig. 5l) returning to positions (Fig. 5j) that confer a closed, non-conducting ion channel. To return back to the resting state, the receptor must undergo conformational rearrangement from the desensitized to the closed, resting state, in a process termed recovery from desensitization[16].

The ATD local dimers maintain their relative positioning between different gating states, resulting in rigid-body movements of the ATD tetramer (Extended Data Fig. 7d–f). During opening, the ATD tetramer rotates by 11° clockwise as viewed extracellularly (Extended Data Fig. 7e). Upon desensitization, the ATD further rotates clockwise by an additional 7° (Extended Data Fig. 7f). To recover from desensitization back to the resting state, the ATD must then rotate counter-clockwise by 18°. Maintenance of the ATD tetrameric arrangement in different gating states[29,40] emphasizes importance of the ATDs for iGluR assembly[41–45],

while enormous rigid body rotations provide a way to fine tune synaptic transmission via altering cross-synaptic interactions[46].

Discussion

The structures of AMPAR complexes allow better understanding of the iGluR gating mechanism (Extended Data Fig. 8). Channel opening in GluA2-STZ$_{Glu+CTZ}$ is accompanied by the outward flipping of Q586, which occludes the channel in the closed state, away from the central pore axis. Therefore, the Q/R site at the tip of M2 seems to function as a lower gate. We propose that individual AMPAR subunit contributions to the lower gate result in the sub-conductance states observed in single-channel AMPAR studies[47,48]. AMPARs occupy their highest conductance state in the presence of glutamate[49,50] and STZ[26]. We expect that the highest conductance state results from all subunits being engaged by glutamate[51,52] when channel occlusion is relieved at both gates. STZ similarly promotes the higher conductance states by stabilizing the open conformation of the lower gate through interaction with the M2 helices. We therefore believe that our GluA2-STZ$_{Glu+CTZ}$ structure represents the maximum-conductance state of the channel.

In addition, the prominent placement of Q586 of the Q/R-site in the ion channel pore explains why AMPARs containing the R-edited GluA2 subunits show dramatically reduced ion channel conductance[53], likely through adding a bulky, charged residue into the permeation pathway. At the level of glutamate receptors, this demonstrates how compartment-specific mRNA editing alters ion channel conductance and AMPAR-mediated excitatory neurotransmission[2]. Importantly, identification of the earlier-predicted[32] M3 kink at A618 in subunits B/D upon channel opening suggests a wider role for A618 across gating in the iGluR family, as it is part of the highly-conserved SYTANLAAF motif[20]. Also in this motif is the Lurcher mutation A622T, which dramatically changes function across iGluR subtypes, resulting in constitutively-activated receptors and dramatically different gating properties[54]. The proximity of this site to A618 suggests that the Lurcher mutation may change iGluR gating through altering the properties of M3 kinking upon channel opening. Better understanding of AMPAR gating and availability of the high-resolution open-state structure will help overcome barriers in therapeutic design and treatment of neurodegenerative diseases.

Methods

Construct

The fusion constructs used for cryo-EM were prepared by introducing a single GT linker between rat GluA2$_{flip}$ construct described in literature[11] and mouse GSG1L truncated after F237[16] or STZ truncated after L207[15], in the pEG BacMam vector[55], with a C-terminal eGFP for FSEC[56] profiling and monitoring during expression, in addition to a streptavidin affinity tag for purification purposes. The amino acids T-G-G were included between the C-terminus of GSG1L or STZ and a thrombin cleavage site (L-V-P-R-G-S) prior to the C-terminal eGFP and affinity tag.

Electrophysiology

DNA encoding wild type GluA2 or GluA2-STZ was introduced into a plasmid for expression in eukaryotic cells that was engineered to produce green fluorescent protein via a downstream internal ribosome entry site[11]. HEK293 cells (ATCC #CRL-1573) grown on glass cover slips in 35 mm dishes were transiently transfected with 1–5 μg of plasmid DNA using Lipofectamine 2000 Reagent (Invitrogen). Recordings were made 24 to 96 hours after transfection at room temperature. Currents from whole cells, typically held at a −60 mV potential, were recorded using Axopatch 200B amplifier (Molecular Devices, LLC), filtered at 5 kHz and digitized at 10 kHz using low-noise data acquisition system Digidata 1440A and pCLAMP software (Molecular Devices, LLC). The external solution contained (in mM): 140 NaCl, 2.4 KCl, 4 $CaCl_2$, 4 $MgCl_2$, 10 HEPES pH 7.3 and 10 glucose; 7 mM NaCl was added to the extracellular activating solution containing 3 mM L-glutamate (Glu). The internal solution contained (in mM): 150 CsF, 10 NaCl, 10 EGTA, 20 HEPES pH 7.3. Rapid solution exchange was achieved with a two-barrel theta glass pipette controlled by a piezoelectric translator. Typical 10–90% rise times were 200–300 μs, as measured from junction potentials at the open tip of the patch pipette after recordings. Data analysis was performed using the computer program Origin 9.1.0 (OriginLab Corp.).

Expression and purification

The GluA2-GSG1L and GluA2-STZ bacmid and baculovirus were made using standard methods[55], and the following methods were applied to the expression and purification of both constructs. P2 virus, produced from Sf9 cells (GIBCO #12659017), was added to HEK293S GnTI⁻ cells (ATCC #CRL-3022) at 37 ˚C and 5% CO_2. At 12 hours post-infection, 10 mM sodium butyrate was added the temperature was changed to 30 ˚C. At 72 hours post-infection, cells were collected by low-speed centrifugation (4,000 rpm, 15 minutes). Cells were then washed with PBS pH 8.0 and pelleted with low speed centrifugation (4,000 rpm, 15 minutes). The washed cells were lysed with a Misonix sonicator (18 x 10s, power level 7) in a 150 mM NaCl, 20 mM Tris-HCl (pH 8.0) containing protease inhibitors (0.8 μM aprotinin, 2 μg/ml leupeptin, 2 μM pepstatin A and 1 mM phenylmethysulfonyl fluoride) – 50 ml was used per 1 L HEK 293 cells. Following, the lysate was clarified after centrifugation (8,000 rpm, 15 minutes), and the membranes were collected by ultracentrifugation (40,000 rpm, 40 minutes). The membranes were collected and mechanically homogenized, then solubilized for two hours in 150 mM NaCl, 20 mM Tris-HCl pH 8.0, 1% digitonin (Cayman Chemical Company #14952). Insoluble material was removed by ultracentrifugation (40,000 rpm, 40 minutes). Streptavidin-linked resin was added to the soluble material (1 ml resin per 1 L cells), and left to bind for 10–14 hours. The resin was washed with 10 column volumes of 150 mM NaCl, 20 mM Tris-HCl pH 8.0, 0.1% digitonin (0.05% digitonin was used in the GluA2-STZ purification). Elution was done with the same buffer but supplemented with 2.5 mM D-desthiobiotin. The sample was then concentrated and digested with thrombin (1:200 mass ratio of thrombin to eluted protein) for 2 hours at 22 ˚C. The sample was then loaded onto a size-exclusion chromatography column (Superose-6) equilibrated with 150 mM NaCl, 20 mM Tris-HCl pH 8.0, 0.1% digitonin (0.05% digitonin was used in the GluA2-STZ purification). The peak fractions were pooled for cryo-EM specimen preparation, and concentrated to 5 mg/ml (4 mg/ml for GluA2-STZ). All steps, unless otherwise noted, were performed at 4 ˚C.

Cultured Cells Details

Human Embryonic Kidney 293 (HEK293) cells were used for patch-clamp electrophysiology. Cells were obtained from ATCC and were not further authenticated. Cells were grown and maintained using standard protocols at 37 C with 5% CO2, in DMEM media (Corning) supplemented with 10% heat inactivated fetal bovine serum (Crystalgen). Before recordings, cells were plated on glass coverslips in 35 mm dishes and transiently transfected with 1–5 mg of plasmid DNA using Lipofectamine 2000 Reagent (Invitrogen). Cells were passed twice a week and were used until the 30th passage.

HEK293S GnTI⁻ cells were used to express protein for cryo-EM. Cells were obtained from ATCC and were not further authenticated. Cells were grown and maintained at 37 C and 5% CO2 using standard protocols, in Freestyle 293 media (GIBCO) supplemented with 2% heat inactivated fetal bovine serum (Crystalgen). Cells were passed twice a week and were used until the 30th passage.

Sf9 insect cells were used to make baculovirus for infecting HEK293S GnTI⁻ cells. Cells were obtained from GIBCO and were not further authenticated. Cells were grown and maintained at 27 C using standard protocols, in Sf-900 III SFM (GIBCO). Cells were passed twice a week and were used until the 30th passage.

Cryo-EM sample preparation and data collection

C-flat (Protochips, Inc., Morrisville, NC) CF-1.2/1.3-2Au 200 mesh holey carbon grids were coated with gold using an Edwards Auto 306 evaporator. Carbon was removed using Ar/O_2 (6 minutes, 50 watts, 35.0 sccm Ar, 11.5 sccm O_2) plasma treatment with a Gatan (Pleasanton, CA, USA) Solarus 950 advanced plasma system, making Au 1.2/1.3 holey /on Au mesh grids[57]. In order to make the surface hydrophilic prior to sample application, the grid surface was plasma-treated with H_2/O_2 (20s, 10 watts, 6.4 sccm H_2, 27.5 sccm O_2). Frozen-hydrated grids were prepared using a Vitrobot Mark IV (FEI, Hillsboro, OR, USA). 3 μl of sample (5 mg/ml GluA2-GSG1L with or without 0.3 mM antagonist ZK200775) was applied to the plasma-treated grids using 3.0 s blotting time, 3 blot force, 30.0 s wait time and 100% humidity at 22 ˚C. For the open state, 4 mg/ml GluA2-STZ was incubated for 15 minutes with 100 μM CTZ, then 3 μl of this was quickly added and pipetted up-and-down in a mixture of 0.5 μl 700 mM glutamate (final concentration 100 mM). 3 μl of this mixture was added to the grid, blotted as described above.

The GluA2-GSG1L data (apo/ZK) were collected on a Tecnai F30 Polara (FEI) microscope operating at 300 kV, using Leginon[58] with a Gatan K2 Summit electron detection (DED) camera (Gatan, Pleasanton, CA, USA) in counting mode with a pixel size of 0.98 Å. Data were collected across 40 frames (0.2 s per frame), with a dose rate of 8 e⁻ pixel⁻¹ s⁻¹ (total dose of ~67 e⁻ Å⁻²), within defocus range −1.5 μm to −3.5 μm, C_s 2.26 mm. The GluA2-STZ data were collected on a Titan Krios microscope (FEI) operating at 300 kV, using Leginon with a post-GIF quantum energy filter (20 eV slit) and Gatan K2 Summit direct camera DED camera in counting mode operating at a pixel size of 1.08 Å/pixel. A dose rate of 8 e⁻ physical pixel⁻¹ s⁻¹ (total dose of ~55 e⁻ Å²) was used across 40 frames (0.2 ms per frame), within the defocus range −1.0 μm to −3.0 μm.

Image processing

All frame alignment and dose-weighting was carried out in MotionCor2[59]. CTF correction, with gCTF[60], was performed on non-dose-weighted micrographs, with all further processing on dose-weighted micrographs using RELION 2.0[61]. From 2,938 micrographs for GluA2-GSG1L bound to ZK, 541,261 particles were picked. The data was binned to 3.92 Å/pixel and subject to 2D classification, which resulted in cleaning the particle pool to 513,406 particles. These particles were then subject to 3D classification without symmetry into ten classes and the GluA2-2xGSG1L$_{ZK}$ model[16] low-pass filtered to 40 Å as a reference. Three classes, with two showing different ECD conformations (i.e., state 1 and state 2) and two auxiliary subunits bound were chosen for additional 3D sub-classification. This resulted in a group of 234,426 particles, which were unbinned to a pixel size of 1.96, and subject to classification with the GluA2-2xGSG1L$_{ZK}$ model (40 Å filter) as the reference. This resulted in two well-structured groups of particles: GluA2-GSG1L$_{ZK-1}$ (26,971 particles) and GluA2-GSG1L$_{ZK-2}$ (41,926 particles). The particles were unbinned to the original 0.98 Å/pixel size, and refined with C2-symmetry. Of note is that we did not observe any stoichiometric heterogeneity, as was observed in cryo-EM performed on the GluA2-GSG1L complex solubilized in DDM[16].

For the GluA2-GSG1L collection in the absence of ligand, 242,078 particles were automatically picked from 2,593 micrographs using six 2D classes as references (generated from manual picking as described above). The particle images were binned to 3.92 Å/pixel, and 235,543 particles remained following 2D classification. Following, 3D classification was carried out without symmetry into ten classes with the 40 Å low-pass filtered GluA2-GSG1L$_{ZK-1}$ map. Six classes, numerating 115,120 particles showed structural details that warranted further image processing. The particles were unbinned to 0.98 Å/pixel and classified in 3D into 10 classes with the GluA2-GSG1L$_{ZK-1}$. Resulting were two prominent classes, GluA2-GSG1L$_{apo-1}$ (20,392 particles) and GluA2-GSG1L$_{apo-2}$ (18,926 particles), which were refined with C2-symmetry, and resemble the two states observed for GluA2-GSG1L in the presence of ZK (Extended Data Figs 3 and 4).

A total of 4,116 micrographs were collected for GluA2-STZ, and 595,889 particles were automatically picked, with manually-picked particles used to generate reference classes as described above. The particles were binned twice to 2.16 Å/pixel and subject to 2D classification, which resulted in 581,495 particles being subject to further image processing. The original GluA2-2xSTZ antagonist-bound map[15], low-pass filtered to 40 Å, was used as a reference model for 3D classification into ten classes without symmetry imposed. 3D classification resulted in 278,454 particles, from four classes, being chosen for further image processing, without observation of stoichiometric heterogeneity as in the DDM-solubilized complex[15], and the particles were unbinned to 1.08 Å/pixel and classified in 3D to ten classes. Particles from three classes, numerating 69,207 particles and showing structurally-similar features, were chosen for refinement. Initial refinement, with C2-symmetry, resulted in a 4.2 Å map, which showed side chain features in the GluA2 core but was lacking details for STZ. To better align particles according to the GluA2 TMD and STZ, we generated a soft spherical mask around the detergent micelle (which encompassed all of the GluA2 and STZ TMDs and STZ extracellular head). This resulted in an overall 4.0 Å map, with distinct

side chain features throughout the TMD for model building of the GluA2 and STZ TMDs. We did not observe a digitonin-bound state of GluA2-STZ$_{Glu+CTZ}$, as we did for GluA2-GSG1L in the resting states (GluA2-GSG1L$_{ZK-2}$, GluA2-GSG1L$_{apo-2}$).

The resolution for all reconstructions was estimated using the FSC=0.143 criterion[62] between independent half maps on corrected FSC curves in which the influences of the mask were removed[63] (Extended Data Fig. 1). All maps were postprocessed using a softmask in RELION, and B-factors for map sharpening were automatically estimated (Extended Data Table 1). All visualization of EM densities was done in UCSF Chimera[64]. Local resolution for each map (Extended Data Fig. 2) was calculated with unfiltered half maps using ResMap[65].

Model Building

To build the state 1 ZK-bound and GluA2-GSG1L models we individually isolated the ATD and LBD dimers, as well as the TMD, from the GluA2-2xGSG1L$_{ZK}$ complex structure[16] using rigid-body fitting in COOT[66]. Side chains in the TMD were defined based on local resolution, as was the structure of the M2 helix and pore loop. The resulting model was refined against an un-filtered half map (work) in real space with constraints using PHENIX[67]. The refined model was tested for overfitting (Extended Data Fig. 2) by shifting the coordinates with shake in PHENIX and building a density in EMAN2[68] from the shaken model. FSC was calculated between the densities from the shaken model, the map used in PHENIX refinement (work), second half map (free) and unfiltered sum map, using EMAN2. The resulting GluA2-GSG1L$_{ZK-1}$ model was used as a basis to build GluA2-GSG1L$_{apo-1}$. Correspondingly, the ATD and LBD local dimers were moved as rigid bodies to define the state 2 models (GluA2-GSG1L$_{ZK-2}$ and GluA2-GSG1L$_{apo-2}$), and features were adjusted manually according to high resolution features in GluA2-GSG1L$_{ZK-2}$. Secondary structure features of the M3 pore were further defined in the GluA2-GSG1L$_{ZK-2}$ M3 density. The resulting models were also real space refined in PHENIX and tested for overfitting (Extended Data Fig. 2). State 2 models were refined in the absence of digitonin.

For GluA2-STZ$_{Glu+CTZ}$, we rigid-body fit the high-resolution structures of the ATD[45] and glutamate/CTZ-bound LBD[35]. We individually rigid body fit helices from the TMD of our GluA2-GSG1L$_{ZK-1}$ refined structure, and rigid-body fit STZ subunits from the GluA2-2xSTZ$_{ZK}$ structure[15] in COOT for an initial model. After increasing the resolution in the TMD map, we built STZ and the GluA2 TMD de novo. The resulting models were also real space refined in PHENIX and tested for overfitting (Extended Data Fig. 2), of which there are no signs of over-fit models. Structures were visualized and figures were prepared in Pymol[67].

Data Availability

Cryo-EM density maps have been deposited in the Electron Microscopy Data Bank (EMDB) under accession numbers EMD-8819 (GluA2-GSG1L$_{ZK-1}$), EMD-8820 (GluA2-GSG1LL$_{ZK-2}$), EMD-8821 (GluA2-GSG1L$_{apo-1}$), EMD-8822 (GluA2-GSG1L$_{apo-2}$), and EMD-8823 (GluA2-STZ$_{Glu+CTZ}$, including directed TMD map). Model coordinates have been deposited in the Protein Data Bank (PDB) under accession numbers 5WEK (GluA2-

GSG1L$_{ZK-1}$), 5WEL (GluA2-GSG1LL$_{ZK-2}$), 5WEM (GluA2-GSG1L$_{apo-1}$), 5WEN (GluA2-GSG1L$_{apo-2}$), and 5WEO (GluA2-STZ$_{Glu+CTZ}$). All other data are available from the corresponding authors upon reasonable request.
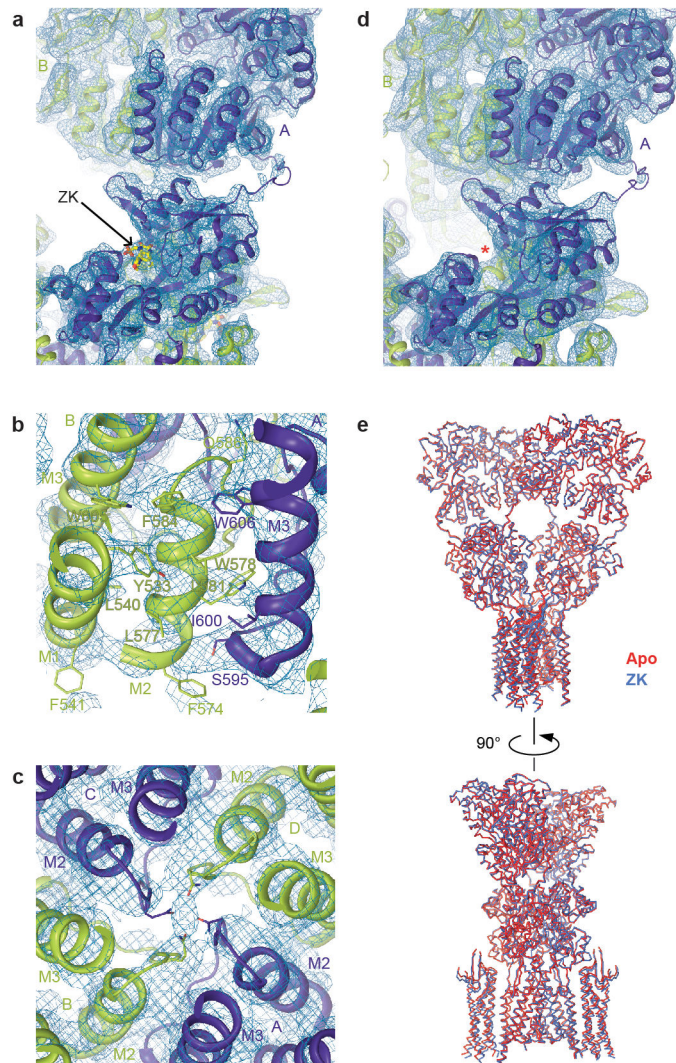
Extended Data
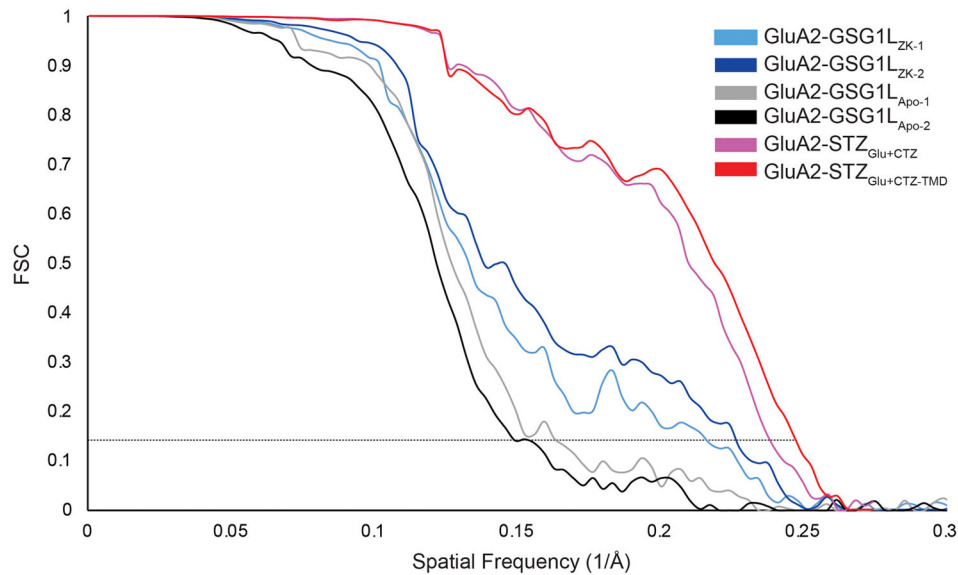
Extended Data Figure 1. FSC curves for cryo-EM reconstructions
Fourier shell correlation (FSC) curves calculated between half-maps for GluA2-GSG1L$_{ZK-1}$, GluA2-GSG1L$_{ZK-2}$, GluA2-GSG1L$_{apo-1}$, GluA2-GSG1L$_{apo-2}$ and GluA2-STZ$_{Glu+CTZ}$ cryo-EM reconstructions, as well as for the GluA2-STZ$_{Glu+CTZ}$ TMD reconstruction from directed refinement. The dashed line indicates FSC=0.143.
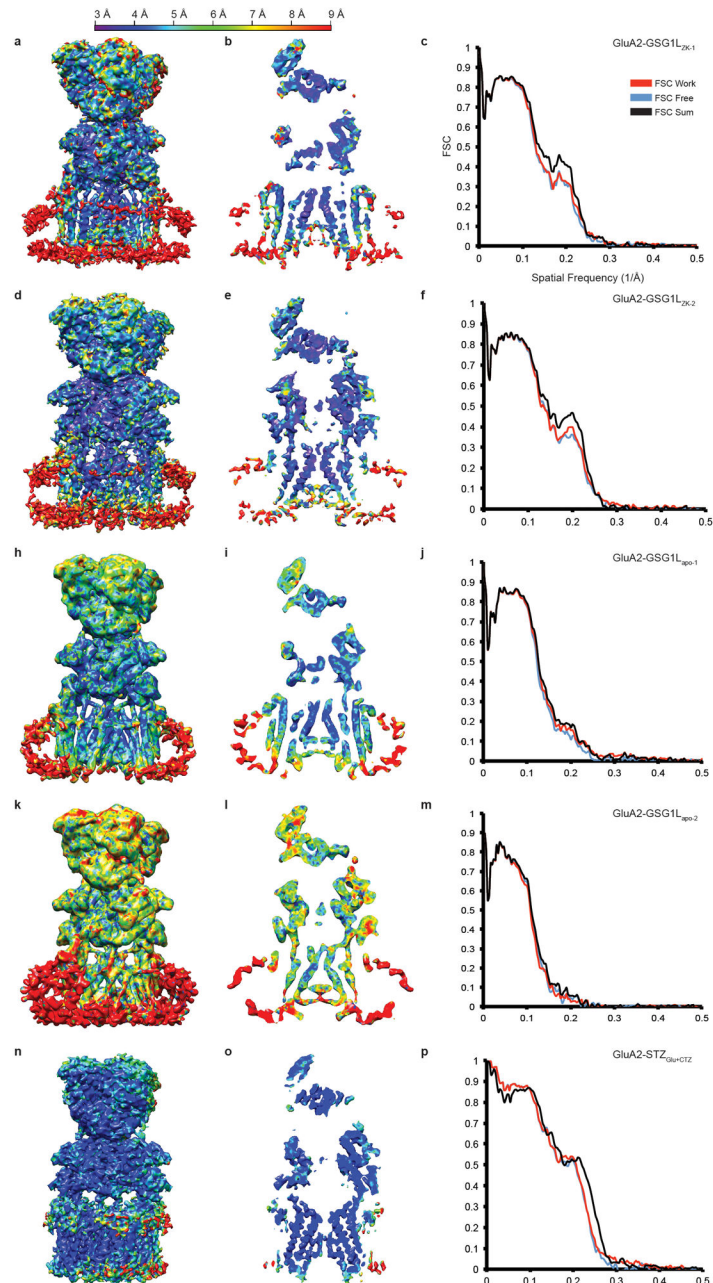
Extended Data Figure 2. Local resolution and fitting of cryo-EM maps
Local resolution calculated using Resmap and two unfiltered halves of the reconstruction for GluA2-GSG1L$_{ZK-1}$, GluA2-GSG1L$_{ZK-2}$, GluA2-GSG1L$_{apo-1}$, GluA2-GSG1L$_{apo-2}$ and GluA2-STZ$_{Glu+CTZ}$ structures viewed parallel to the membrane as a surface (**a, d, h, k, n**) and slice through the center of the receptor (**b, e, i, l, o**), with the cross-validation FSC curves for the refined model versus unfiltered half maps (one used in the refinement, work, and another one not, free) and the unfiltered summed maps shown on the right (**c, f, j, m, p**).
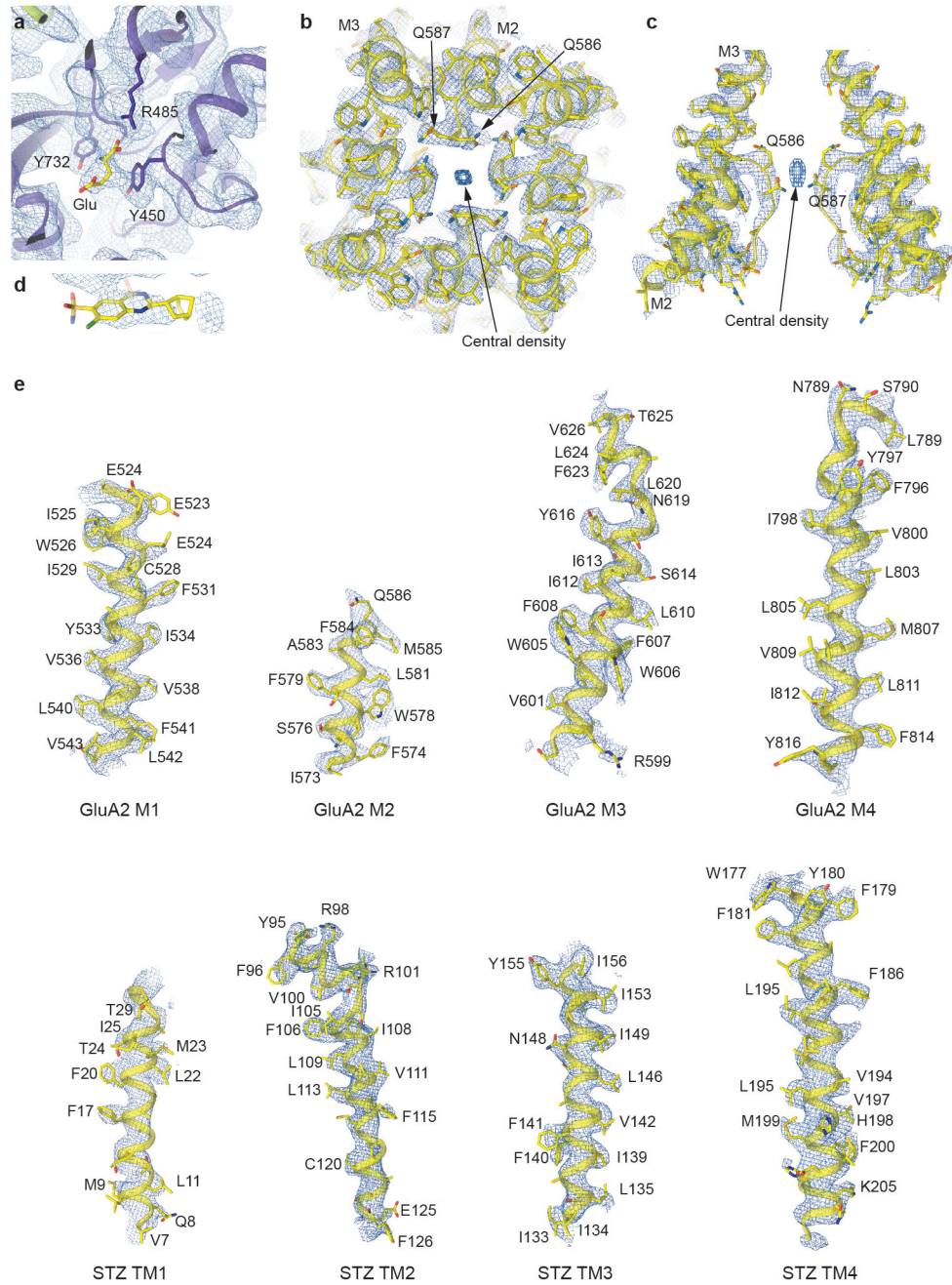
Extended Data Figure 3. Closed state 1 cryo-EM density and comparison of ZK-bound and apo states

a–d, Fragments of GluA2-GSG1L$_{ZK-1}$ and GluA2-GSG1L$_{apo-1}$ with the corresponding cryo-EM density: (**a,d**) ATD and LBD of subunit A in GluA2-GSG1L$_{ZK-1}$ (**a**) and GluA2-GSG1L$_{Apo-1}$ (**d**) with density for ZK indicated in the GluA2-2xGSG1L$_{ZK-1}$ structure; (**b**) M2 helix and (**c**) selectivity filter with the Q/R-site Q586 side chains pointing towards the center of the pore in GluA2-GSG1L$_{ZK-1}$. **e**, Superposition of GluA2-GSG1L$_{ZK-1}$ (blue) and GluA2-GSG1L$_{apo-1}$ (red) viewed parallel to the membrane. Note, the structures are almost indistinguishable (RMSD = 0.526 Å). Densities are shown at 6 σ.
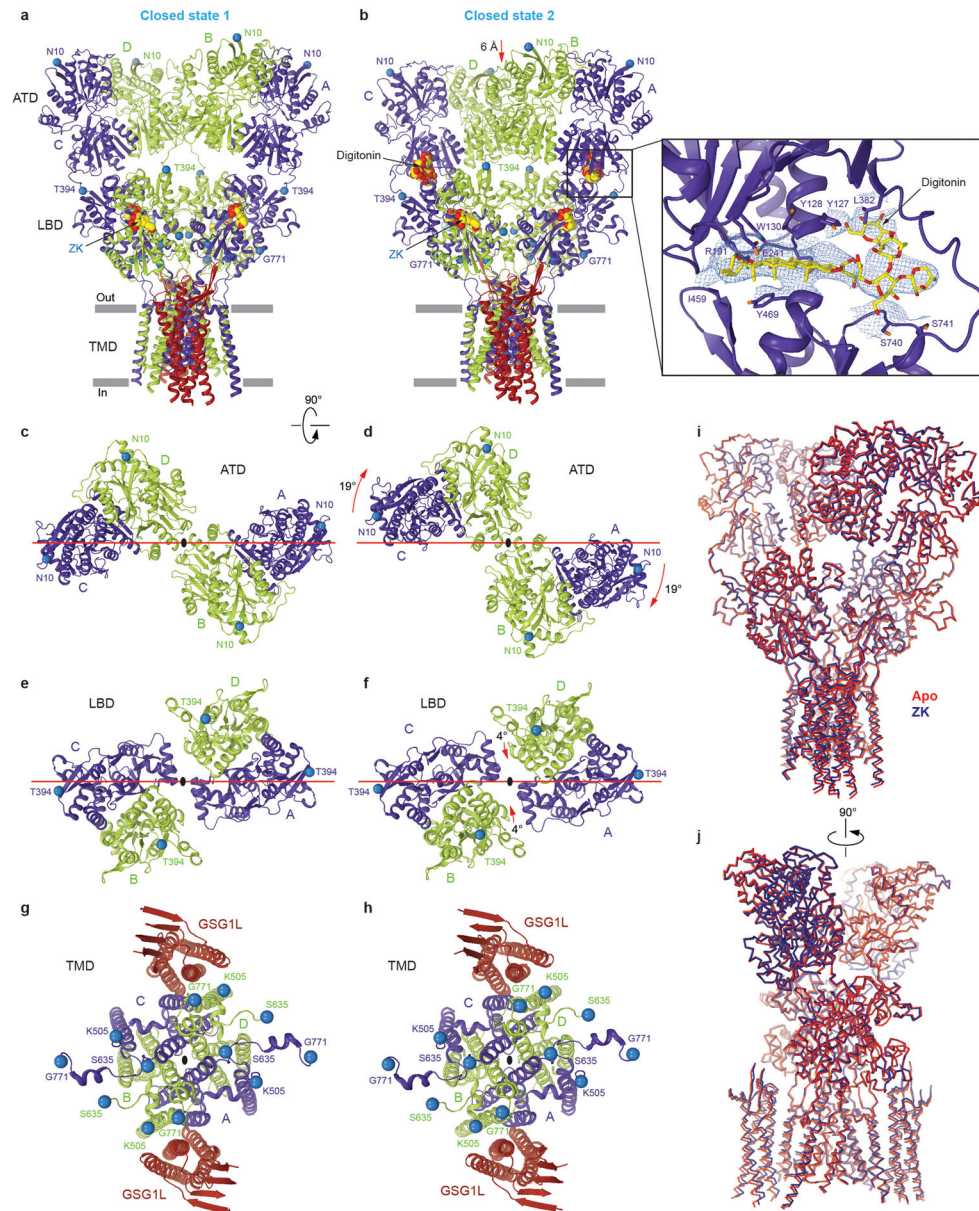
**Extended Data Figure 4. Closed state 2 structure and digitonin binding pocket**

a–b, Structures of GluA2-GSG1L$_{ZK-1}$ (**a**) and GluA2-GSG1L$_{ZK-2}$ (**b**) viewed parallel to the membrane. The GluA2 subunits A and C are colored purple, B and D green and GSG1L red. The competitive antagonist ZK and digitonin are shown as space-filling models. In **b**, inset shows expanded view of the boxed region, demonstrating cryo-EM density for digitonin (blue mesh, 4 σ). Digitonin and the surrounding residues in the inset are shown in stick representation. **c–h**, Top down views along the axis of the overall 2-fold rotational symmetry on the ATD (**c–d**), LBD (**e–f**) and TMD (**g–h**) layers. Rigid-body rotation of the ATD tetramer in (**d**) and rotation of LBD dimers in (**f**) are indicated by red arrows. (**i–j**) Superposition of GluA2-GSG1L$_{ZK-2}$ (blue) and GluA2-GSG1L$_{Apo-2}$ (red) viewed parallel to the membrane. Note, the structures are almost indistinguishable (RMSD = 0.701 Å).

**Extended Data Figure 5. Cryo-EM density for the open state**

a–f, Fragments of GluA2-STZ$_{Glu+CTZ}$ with the corresponding cryo-EM density: (**a**) zoom on the glutamate binding pocket, (**b–c**) ion channel pore with a central density at the selectivity filter, likely for a sodium ion that is hydrated based on the pore diameter, viewed (**b**) from the top of the selectivity filter looking down into the cytoplasm or (**c**) parallel to the membrane with two distal and proximal GluA2 subunits removed, (**d**) density for CTZ and (**e**) transmembrane domain segments for GluA2 (upper row) and STZ (lower row).
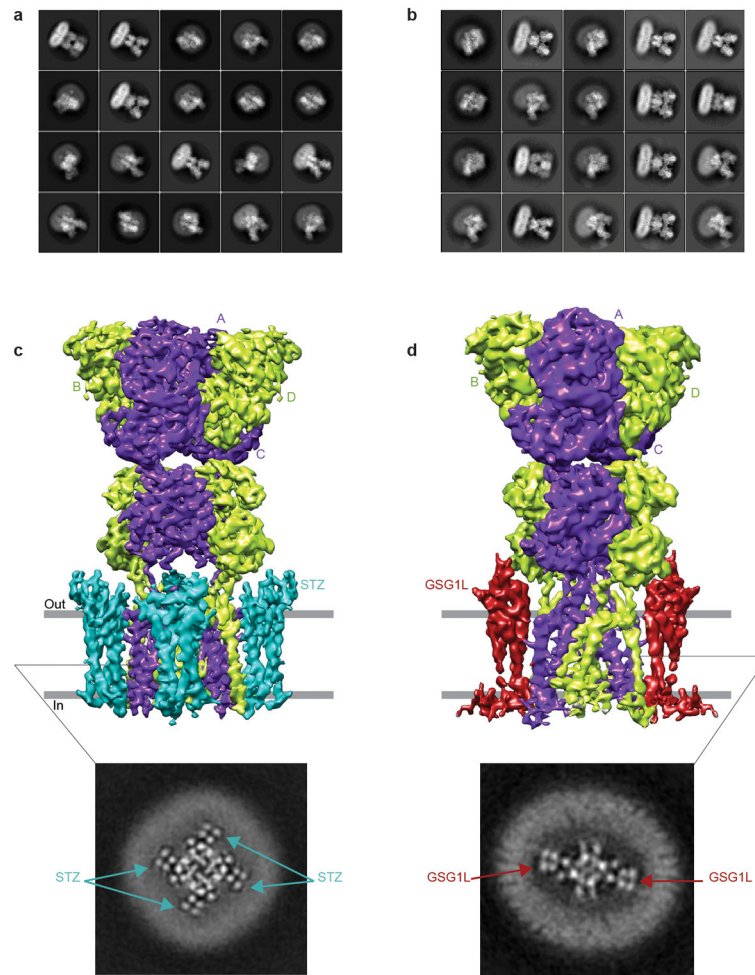
Extended Data Figure 6. Overview of single-particle cryo-EM and stoichiometry for GluA2-STZ and GluA2-GSG1L solubilized in digitonin

a–b, Two-dimensional class averages for GluA2-STZ$_{Glu+CTZ}$ (**a**) and GluA2-GSG1L$_{ZK}$ (**b**) indicating 3-layer architecture of the particles. **c–d**, Final densities for GluA2-STZ$_{Glu+CTZ}$ (**c**) and GluA2-GSG1L$_{ZK-1}$ (**d**) with the GluA2 subunits A and C colored purple, B and D green, STZ cyan and GSG1L red. Insets show 2D slices made parallel to the membrane through the refined, nonfiltered map. Note, while four STZ molecules bind one receptor, only two copies of GSG1L can bind per GluA2 tetramer.
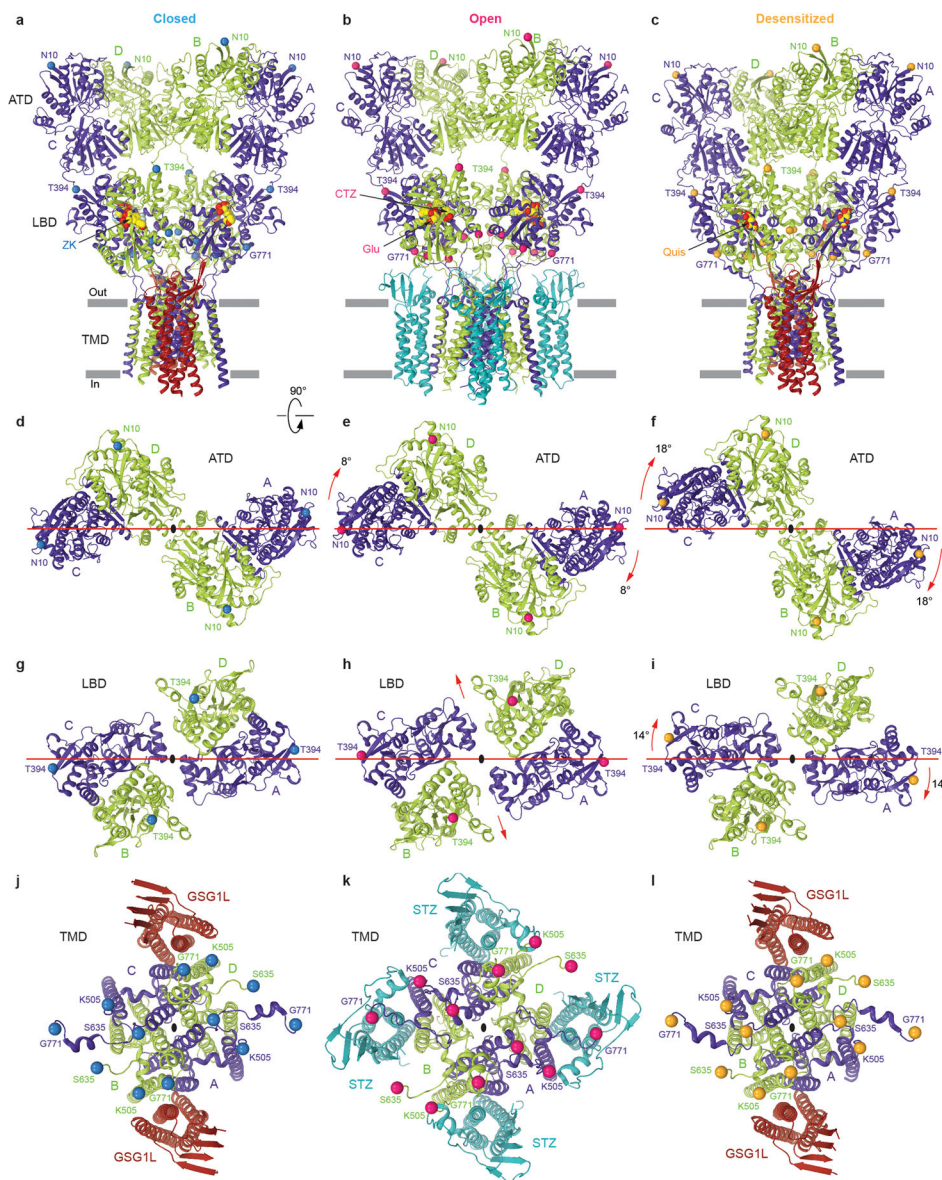
Extended Data Figure 7. Conformational differences between the closed, open and desensitized states

a–c, Structures of GluA2-GSG1L$_{ZK-1}$ in the closed state (**a**), GluA2-STZ$_{Glu+CTZ}$ in the open state (**b**) and GluA2-2xGSG1L$_{Quis}$ in the desensitized state (**c**) viewed parallel to the membrane. The GluA2 subunits A and C are colored purple, B and D green, GSG1L red and STZ cyan. The competitive antagonist ZK, agonists Glu and Quis and positive allosteric modulator CTZ are shown as space-filling models. (**d–l**), Top down views along the axis of the overall 2-fold rotational symmetry on the layers of ATD (**d–f**), LBD (**g–i**) and TMD (**j–l**). Rigid-body rotation of the ATD tetramers in (**e**) and (**f**), broadening of LBD layer in (**h**) and rotation of subunit A/C LBDs in (**i**) are indicated by red arrows. Note, dramatic opening in the middle of the LBD layer (**h**) and pore dilation (**k**) in the open state.
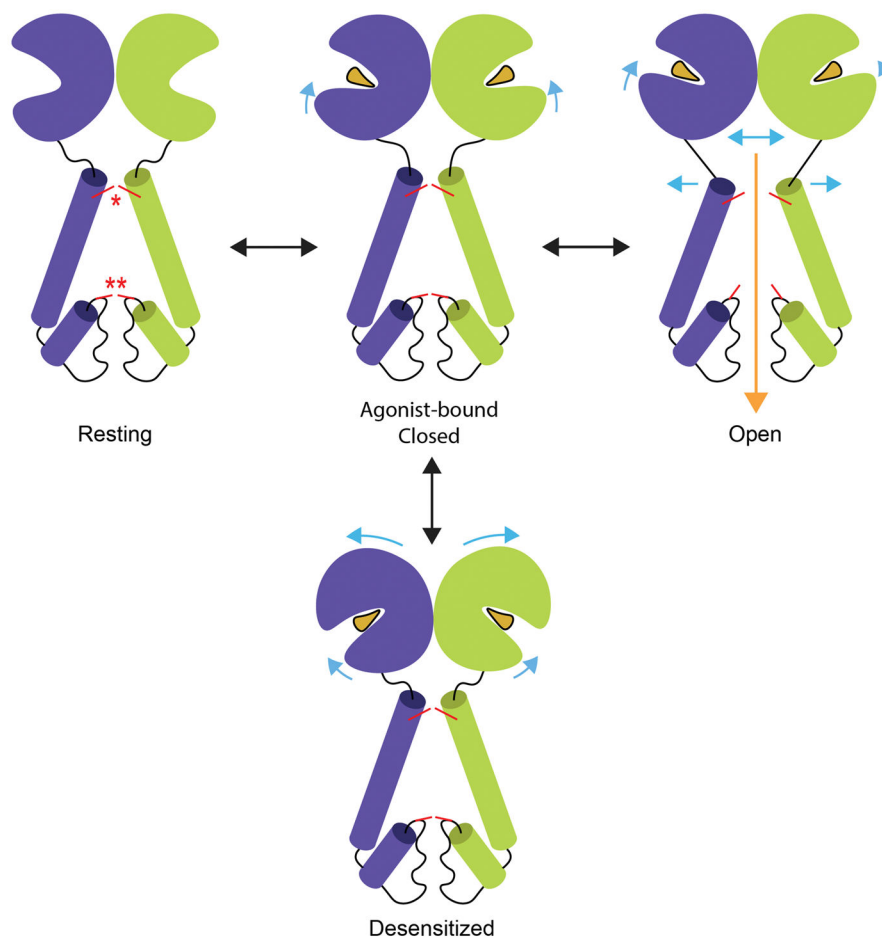
Extended Data Figure 8. iGluR Gating Mechanism

Two of four iGluR subunits are shown with the ATDs omitted. Four basic states of iGluR gating are illustrated: Resting, represented by apo (GluA2-GSG1L$_{apo-1}$) or antagonist-bound closed state (GluA2-GSG1L$_{ZK-1}$) structures; Closed, agonist-bound (pre-active state crystal structures[10,11]); Open (GluA2-STZ$_{Glu+CTZ}$) and Desensitized (GluA2-2xGSG1L$_{Quis}$ complex[16]). Transitions between the states are indicated by black arrows, conformational rearrangements by blue arrows and ionic current through the open channel by an orange arrow. Upper and lower gates are indicated by one and two red asterisks, respectively, with red sticks at the upper gate representing channel occluding residues at the bundle crossing and the Q/R site at the lower gate. Glutamate molecules are illustrated by orange wedges. The receptor sits in a resting, closed state, with its LBD clamshells in the maximally open conformations, unoccupied by the neurotransmitter glutamate. Upon glutamate binding, the LBD clamshells close, as described in the pre-activated crystal structures, to an intermediate state that does not put enough strain on the LBD-TMD linkers to open the channel. The LBDs then transition to their maximally-closed state, which strains the LBD-TMD linkers, causing the channel pore to open and conduct ions. Most AMPA receptors, however, quickly desensitize, transitioning to the desensitized state from the open state via the agonist-bound, closed state. Desensitization is accompanied by the rupture of the upper LBD interfaces,

with the LBDs adapting their maximally closed clamshell conformations, as described in the desensitized-state GluA2-GSG1L complex.

Extended Data Table 1

Cryo-EM data collection, refinement and validation statistics.

	GluA2-GSG1L$_{ZK-1}$ (EMDB-8819) (PDB 5WEK)	GluA2-GSG1L$_{ZK-2}$ (EMDB-8820) (PDB 5WEL)	GluA2-GSG1L$_{apo-1}$ (EMDB-8821) (PDB 5WEM)	GluA2-GSG1L$_{apo-2}$ (EMDB-8822) (PDB 5WEN)	GluA2-STZ$_{Glu+CTZ}$ (EMDB-8823) (PDB 5WEO)
Data collection and processing					
Magnification	39,000x		39,000x		130,000x
Voltage (kV)	300		300		300
Electron exposure (e⁻/Å²)	67		67		55
Defocus range (μm)	−1.5 to −3.5		1.5 to −3.5		−1.0 to −3.0
Pixel size (Å)	0.98		0.98		1.08
Symmetry imposed	C2		C2		C2
Initial particle images (no.)	541,261		242,078		595,889
Final particle images (no.)	26,971	41,926	20,392	18,926	69,207
Map resolution (Å) FSC=0.143	4.6	4.4	6.1	6.8	4.2
Map resolution range (Å)	3 to 9	3 to 9	4 to 9	4 to 9	3 to 9
Refinement					
Initial model used (PDB code)	5VHY	5VHY	5VHY	5VHY	5KBU
Model resolution (Å) FSC=0.143	4.6	4.4	6.1	6.8	4.2
Model resolution range (Å)	3 to 9	3 to 9	4 to 9	4 to 9	3 to 9
Map sharpening B factor (Å²)	−172	−196	−225	−653	−160
Model composition					
Non-hydrogen atoms	27,468	27,468	27,360	27,360	30,940
Protein residues	27,360	27,360	27,360	27,360	30,804
Ligands	108	108	N/A	N/A	136
B factors (Å²)					
Protein	263.37	248.89	337.97	409.74	240.10
Ligand	217.60	88.03	N/A	N/A	113.71
R.m.s. deviations					
Bond lengths (Å)	0.01	0.01	0.01	0.01	0.01
Bond angles (°)	1.18	1.25	1.37	1.25	1.16
Validation					
MolProbity score	1.69	1.81	1.85	1.86	2.00
Clashscore	6.12	6.79	7.83	7.84	9.25
Poor rotamers (%)	0.23	0.34	0.14	0.37	0.59
Ramachandran plot					
Favored (%)	93.11	93.22	93.48	93.34	91.10

	GluA2-GSG1L$_{ZK-1}$ (EMDB-8819) (PDB 5WEK)	GluA2-GSG1L$_{ZK-2}$ (EMDB-8820) (PDB 5WEL)	GluA2-GSG1L$_{apo-1}$ (EMDB-8821) (PDB 5WEM)	GluA2-GSG1L$_{apo-2}$ (EMDB-8822) (PDB 5WEN)	GluA2-STZ$_{Glu+CTZ}$ (EMDB-8823) (PDB 5WEO)
Allowed (%)	5.48	6.63	6.34	6.55	8.20
Outliers (%)	1.42	0.14	0.17	0.12	0.70

Supplementary Material

Refer to Web version on PubMed Central for supplementary material.

Acknowledgments

References

1. Kumar J, Mayer ML. Functional insights from glutamate receptor ion channel structures. Annu Rev Physiol. 2013; 75:313–337. [PubMed: 22974439]

2. Traynelis SF, et al. Glutamate receptor ion channels: structure, regulation, and function. Pharmacol Rev. 2010; 62:405–496. [PubMed: 20716669]

3. Bowie D. Ionotropic glutamate receptors & CNS disorders. CNS Neurol Disord Drug Targets. 2008; 7:129–143. [PubMed: 18537642]

4. Chater TE, Goda Y. The role of AMPA receptors in postsynaptic mechanisms of synaptic plasticity. Frontiers in cellular neuroscience. 2014; 8:401. [PubMed: 25505875]

5. Henley JM, Wilkinson KA. Synaptic AMPA receptor composition in development, plasticity and disease. Nature reviews. Neuroscience. 2016; 17:337–350. [PubMed: 27080385]

6. Sobolevsky AI. Structure and gating of tetrameric glutamate receptors. J Physiol. 2015; 593:29–38. [PubMed: 25556785]

7. Mayer ML. Structural biology of glutamate receptor ion channel complexes. Curr Opin Struct Biol. 2016; 41:119–127. [PubMed: 27454049]

8. Sobolevsky AI, Rosconi MP, Gouaux E. X-ray structure, symmetry and mechanism of an AMPA-subtype glutamate receptor. Nature. 2009; 462:745–756. [PubMed: 19946266]

9. Chen L, Durr KL, Gouaux E. X-ray structures of AMPA receptor-cone snail toxin complexes illuminate activation mechanism. Science. 2014; 345:1021–1026. [PubMed: 25103405]

10. Durr KL, et al. Structure and Dynamics of AMPA Receptor GluA2 in Resting, Pre-Open, and Desensitized States. Cell. 2014; 158:778–792. [PubMed: 25109876]

11. Yelshanskaya MV, Li M, Sobolevsky AI. Structure of an agonist-bound ionotropic glutamate receptor. Science. 2014; 345:1070–1074. [PubMed: 25103407]

12. Yelshanskaya MV, et al. Structural bases of noncompetitive inhibition of AMPA subtype ionotropic glutamate receptors by antiepileptic drugs. Neuron. 2016; 91:1–11. [PubMed: 27387643]

13. Herguedas B, et al. Structure and organization of heteromeric AMPA-type glutamate receptors. Science. 2016; 352:aad3873. [PubMed: 26966189]

14. Meyerson JR, et al. Structural mechanism of glutamate receptor activation and desensitization. Nature. 2014; 514:328–334. [PubMed: 25119039]

15. Twomey EC, Yelshanskaya MV, Grassucci RA, Frank J, Sobolevsky AI. Elucidation of AMPA receptor-stargazin complexes by cryo-electron microscopy. Science. 2016; 353:83–86. [PubMed: 27365450]

16. Twomey EC, Yelshanskaya MV, Grassucci RA, Frank J, Sobolevsky AI. Structural Bases of Desensitization in AMPA Receptor-Auxiliary Subunit Complexes. Neuron. 2017; 94:569–580. [PubMed: 28472657]

17. Zhao Y, Chen S, Yoshioka C, Baconguis I, Gouaux E. Architecture of fully occupied GluA2 AMPA receptor-TARP complex elucidated by cryo-EM. Nature. 2016; 536:108–111. [PubMed: 27368053]

18. Doyle DA, et al. The structure of the potassium channel: molecular basis of K+ conduction and selectivity. Science. 1998; 280:69–77. [PubMed: 9525859]

19. Cao E, Liao M, Cheng Y, Julius D. TRPV1 structures in distinct conformations reveal activation mechanisms. Nature. 2013; 504:113–118. [PubMed: 24305161]

20. Huettner JE. Glutamate receptor pores. J Physiol. 2015; 593:49–59. [PubMed: 25556787]

21. Wilding TJ, Lopez MN, Huettner JE. Radial symmetry in a chimeric glutamate receptor pore. Nature communications. 2014; 5:3349.

22. Lopez MN, Wilding TJ, Huettner JE. Q/R site interactions with the M3 helix in GluK2 kainate receptor channels revealed by thermodynamic mutant cycles. J Gen Physiol. 2013; 142:225–239. [PubMed: 23940260]

23. Chang P, et al. Seizure control by decanoic acid through direct AMPA receptor inhibition. Brain. 2016; 139:431–443. [PubMed: 26608744]

24. Chang P, et al. Seizure control by derivatives of medium chain fatty acids associated with the ketogenic diet show novel branching-point structure for enhanced potency. J Pharmacol Exp Ther. 2015; 352:43–52. [PubMed: 25326131]

25. Priel A, et al. Stargazin reduces desensitization and slows deactivation of the AMPA-type glutamate receptors. J Neurosci. 2005; 25:2682–2686. [PubMed: 15758178]

26. Tomita S, et al. Stargazin modulates AMPA receptor gating and trafficking by distinct domains. Nature. 2005; 435:1052–1058. [PubMed: 15858532]

27. MacLean DM, Ramaswamy SS, Du M, Howe JR, Jayaraman V. Stargazin promotes closure of the AMPA receptor ligand-binding domain. J Gen Physiol. 2014; 144:503–512. [PubMed: 25422502]

28. Patneau DK, Vyklicky L Jr, Mayer ML. Hippocampal neurons exhibit cyclothiazide-sensitive rapidly desensitizing responses to kainate. J Neurosci. 1993; 13:3496–3509. [PubMed: 7688040]

29. Yelshanskaya MV, Saotome K, Singh AK, Sobolevsky AI. Probing Intersubunit Interfaces in AMPA-subtype Ionotropic Glutamate Receptors. Sci Rep. 2016; 6:19082. [PubMed: 26739260]

30. Jiang Y, et al. The open pore conformation of potassium channels. Nature. 2002; 417:523–526. [PubMed: 12037560]

31. Long SB, Campbell EB, Mackinnon R. Crystal structure of a mammalian voltage-dependent Shaker family K+ channel. Science. 2005; 309:897–903. [PubMed: 16002581]

32. Sobolevsky AI, Yelshansky MV, Wollmuth LP. The outer pore of the glutamate receptor channel has 2-fold rotational symmetry. Neuron. 2004; 41:367–378. [PubMed: 14766176]

33. Yelshanskaya MV, Mesbahi-Vasey S, Kurnikova MG, Sobolevsky AI. Role of the Ion Channel Extracellular Collar in AMPA Receptor Gating. Sci Rep. 2017; 7:1050. [PubMed: 28432359]

34. Armstrong N, Gouaux E. Mechanisms for activation and antagonism of an AMPA-sensitive glutamate receptor: crystal structures of the GluR2 ligand binding core. Neuron. 2000; 28:165–181. [PubMed: 11086992]

35. Sun Y, et al. Mechanism of glutamate receptor desensitization. Nature. 2002; 417:245–253. [PubMed: 12015593]

36. Armstrong N, Jasti J, Beich-Frandsen M, Gouaux E. Measurement of conformational changes accompanying desensitization in an ionotropic glutamate receptor. Cell. 2006; 127:85–97. [PubMed: 17018279]

37. Salussolia CL, et al. Interaction of the M4 segment with other transmembrane segments is required for surface expression of mammalian alpha-amino-3-hydroxy-5-methyl-4-isoxazolepropionic acid (AMPA) receptors. J Biol Chem. 2011; 286:40205–40218. [PubMed: 21930708]

38. Salussolia CL, et al. A eukaryotic specific transmembrane segment is required for tetramerization in AMPA receptors. J Neurosci. 2013; 33:9840–9845. [PubMed: 23739980]

39. Gan Q, Dai J, Zhou HX, Wollmuth LP. The Transmembrane Domain Mediates Tetramerization of alpha-Amino-3-hydroxy-5-methyl-4-isoxazolepropionic Acid (AMPA) Receptors. J Biol Chem. 2016; 291:6595–6606. [PubMed: 26839312]

40. Shaikh SA, et al. Stargazin Modulation of AMPA Receptors. Cell Rep. 2016; 17:328–335. [PubMed: 27705782]

41. Leuschner WD, Hoch W. Subtype-specific assembly of alpha-amino-3-hydroxy-5-methyl-4-isoxazole propionic acid receptor subunits is mediated by their n-terminal domains. J Biol Chem. 1999; 274:16907–16916. [PubMed: 10358037]

42. Papadakis M, Hawkins LM, Stephenson FA. Appropriate NR1-NR1 disulfide-linked homodimer formation is requisite for efficient expression of functional, cell surface N-methyl-D-aspartate NR1/NR2 receptors. J Biol Chem. 2004; 279:14703–14712. [PubMed: 14732708]

43. Ayalon G, Segev E, Elgavish S, Stern-Bach Y. Two regions in the N-terminal domain of ionotropic glutamate receptor 3 form the subunit oligomerization interfaces that control subtype-specific receptor assembly. J Biol Chem. 2005; 280:15053–15060. [PubMed: 15703162]

44. Ayalon G, Stern-Bach Y. Functional assembly of AMPA and kainate receptors is mediated by several discrete protein-protein interactions. Neuron. 2001; 31:103–113. [PubMed: 11498054]

45. Jin R, et al. Crystal structure and association behaviour of the GluR2 amino-terminal domain. Embo J. 2009; 28:1812–1823. [PubMed: 19461580]

46. Watson JF, Ho H, Greger IH. Synaptic transmission and plasticity require AMPA receptor anchoring via its N-terminal domain. eLife. 2017; 6:e23024. [PubMed: 28290985]

47. Cull-Candy SG, Usowicz MM. Multiple-conductance channels activated by excitatory amino acids in cerebellar neurons. Nature. 1987; 325:525–528. [PubMed: 2433594]

48. Jahr CE, Stevens CF. Glutamate activates multiple single channel conductances in hippocampal neurons. Nature. 1987; 325:522–525. [PubMed: 2433593]

49. Rosenmund C, Stern-Bach Y, Stevens CF. The tetrameric structure of a glutamate receptor channel. Science. 1998; 280:1596–1599. [PubMed: 9616121]

50. Smith TC, Howe JR. Concentration-dependent substate behavior of native AMPA receptors. Nat Neurosci. 2000; 3:992–997. [PubMed: 11017171]

51. Poon K, Ahmed AH, Nowak LM, Oswald RE. Mechanisms of modal activation of GluA3 receptors. Mol Pharmacol. 2011; 80:49–59. [PubMed: 21464198]

52. Prieto ML, Wollmuth LP. Gating modes in AMPA receptors. J Neurosci. 2010; 30:4449–4459. [PubMed: 20335481]

53. Swanson GT, Kamboj SK, Cull-Candy SG. Single-channel properties of recombinant AMPA receptors depend on RNA editing, splice variation, and subunit composition. J Neurosci. 1997; 17:58–69. [PubMed: 8987736]

54. Kohda K, Wang Y, Yuzaki M. Mutation of a glutamate receptor motif reveals its role in gating and delta2 receptor channel properties. Nat Neurosci. 2000; 3:315–322. [PubMed: 10725919]

55. Goehring A, et al. Screening and large-scale expression of membrane proteins in mammalian cells for structural studies. Nat Protoc. 2014; 9:2574–2585. [PubMed: 25299155]

56. Kawate T, Gouaux E. Fluorescence-detection size-exclusion chromatography for precrystallization screening of integral membrane proteins. Structure. 2006; 14:673–681. [PubMed: 16615909]

57. Russo CJ, Passmore LA. Ultrastable gold substrates for electron cryomicroscopy. Science. 2014; 346:1377–1380. [PubMed: 25504723]

58. Suloway C, et al. Automated molecular microscopy: the new Leginon system. J Struct Biol. 2005; 151:41–60. [PubMed: 15890530]

59. Zheng SQ, et al. MotionCor2: anisotropic correction of beam-induced motion for improved cryo-electron microscopy. Nat Methods. 2017; 14:331–332. [PubMed: 28250466]

60. Zhang K. Gctf: Real-time CTF determination and correction. J Struct Biol. 2016; 193:1–12. [PubMed: 26592709]

61. Kimanius D, Forsberg BO, Scheres SH, Lindahl E. Accelerated cryo-EM structure determination with parallelisation using GPUs in RELION-2. eLife. 2016; 5:e18722. [PubMed: 27845625]

62. Scheres SH, Chen S. Prevention of overfitting in cryo-EM structure determination. Nat Methods. 2012; 9:853–854. [PubMed: 22842542]

63. Chen S, et al. High-resolution noise substitution to measure overfitting and validate resolution in 3D structure determination by single particle electron cryomicroscopy. Ultramicroscopy. 2013; 135:24–35. [PubMed: 23872039]

64. Pettersen EF, et al. UCSF Chimera--a visualization system for exploratory research and analysis. J Comput Chem. 2004; 25:1605–1612. [PubMed: 15264254]

65. Kucukelbir A, Sigworth FJ, Tagare HD. Quantifying the local resolution of cryo-EM density maps. Nat Methods. 2014; 11:63–65. [PubMed: 24213166]

66. Emsley P, Lohkamp B, Scott WG, Cowtan K. Features and development of Coot. Acta Crystallogr D Biol Crystallogr. 2010; 66:486–501. [PubMed: 20383002]

67. Afonine PV, et al. Towards automated crystallographic structure refinement with phenix.refine. Acta Crystallogr D Biol Crystallogr. 2012; 68:352–367. [PubMed: 22505256]

68. Tang G, et al. EMAN2: an extensible image processing suite for electron microscopy. J Struct Biol. 2007; 157:38–46. [PubMed: 16859925]
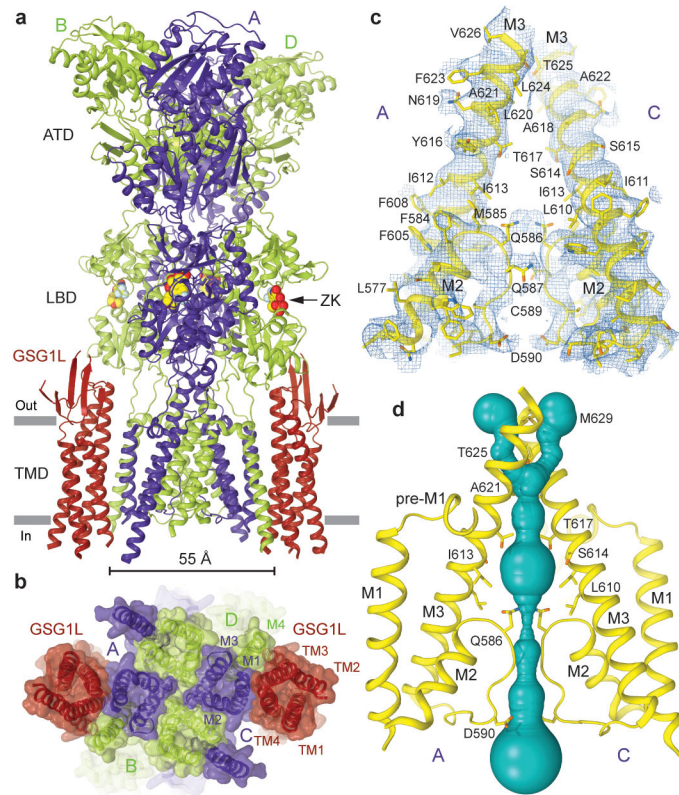
Figure 1. GluA2-GSG1L and ion channel structure

a–b, Model of GluA2-2xGSG1L$_{ZK-1}$ viewed (**a**) parallel to or (**b**) from the intracellular side of the membrane with GluA2 subunits A and C colored purple, B and D green and GSG1L red. The competitive antagonists ZK200775 are shown as space-filling models. **c**, Close-up view of the pore-lining domains M2 and M3 in subunits A and C with cryo-EM density shown as blue mesh. **d**, Ion conduction pathway (violet) with pore-lining residues in the M2 and M3 segments of subunits A and C shown as sticks.
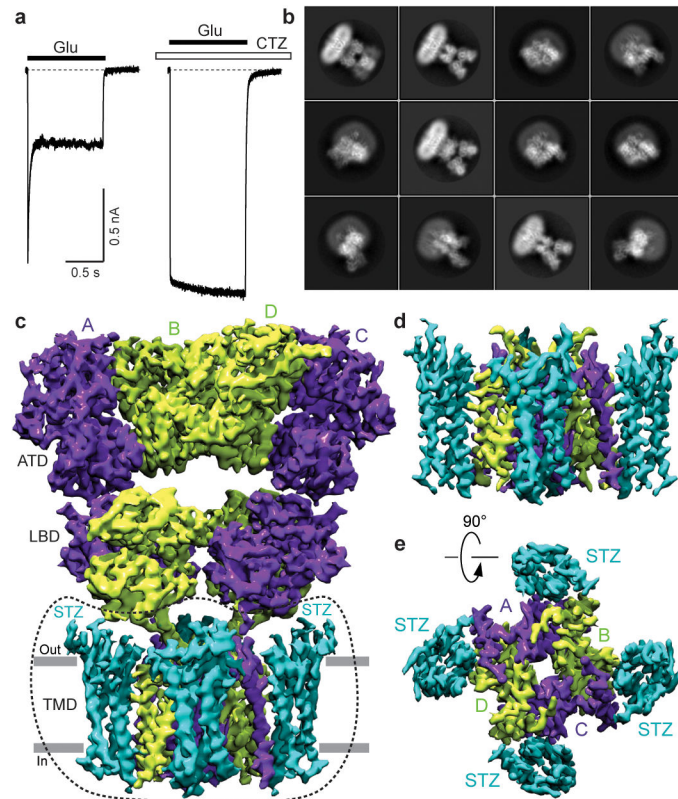
Figure 2. Cryo-EM of an activated GluA2-STZ complex

a, Representative whole-cell currents recorded at −60 mV membrane potential from a HEK 293 cell expressing GluA2-STZ in response to 1 s applications of Glu alone or in the continuous presence of 30 μM CTZ. **b**, Two-dimensional class averages of GluA2-STZ$_{Glu+CTZ}$ particles, showing diverse orientations. **c**, 4.2 Å cryo-EM reconstruction of the entire GluA2-STZ$_{Glu+STZ}$ complex, with GluA2 subunits colored green and purple, and STZ in blue; viewed perpendicular to the membrane. The dashed outline highlights the area focused on in directed refinement to improve the TMD density. **d–e**, Density of the GluA2-STZ$_{Glu+CTZ}$ TMD at 4.0 Å resolution from directed refinement, viewed parallel (**d**) and perpendicular (**e**) to the membrane.
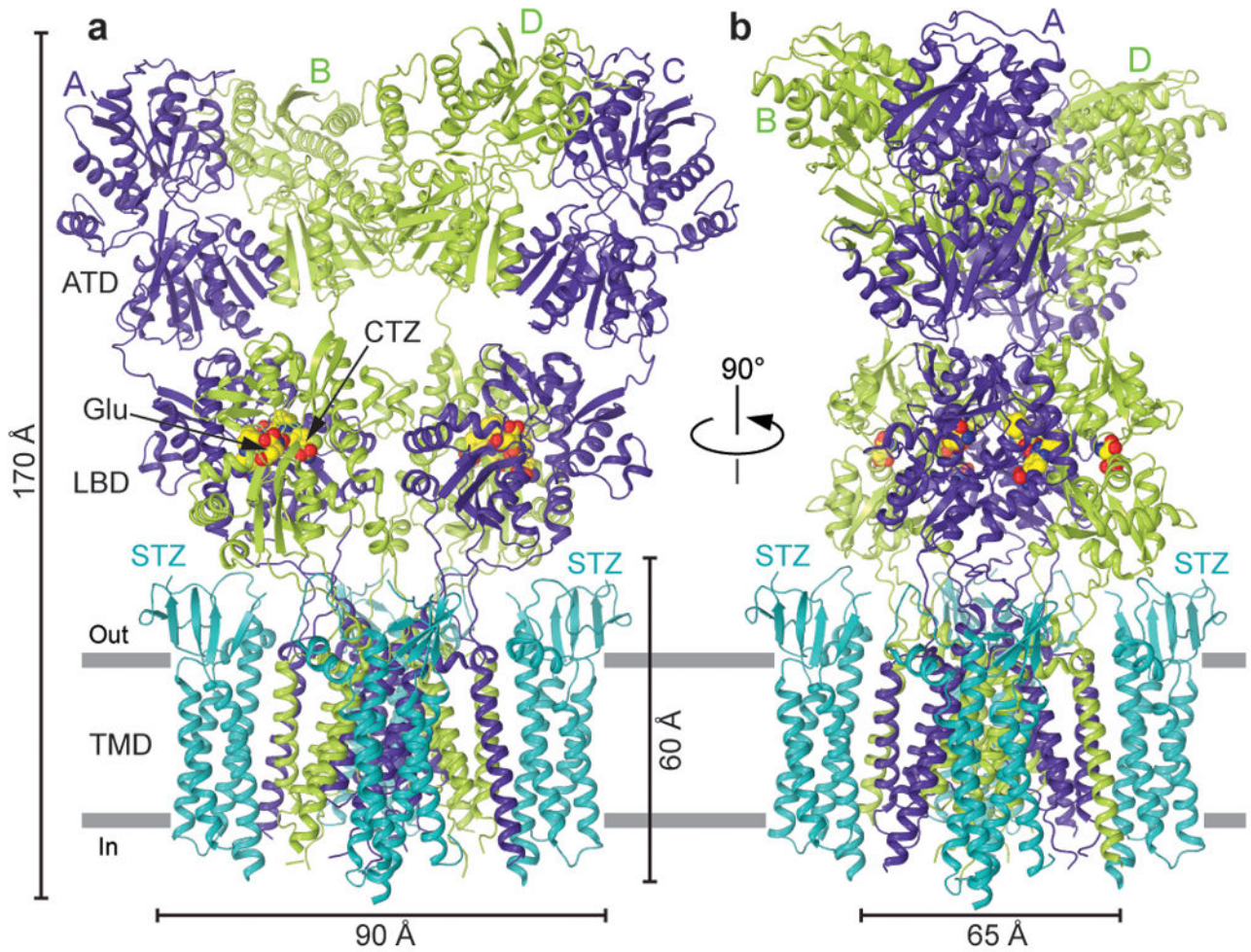
Figure 3. Structure of the GluA2-STZ complex

a–b, Model of GluA2-4xSTZ$_{Glu+CTZ}$ viewed parallel to the membrane with GluA2 subunits A and C colored purple, B and D green and STZ cyan. The molecules of agonist Glu and positive allosteric modulator CTZ are shown as space-filling models.
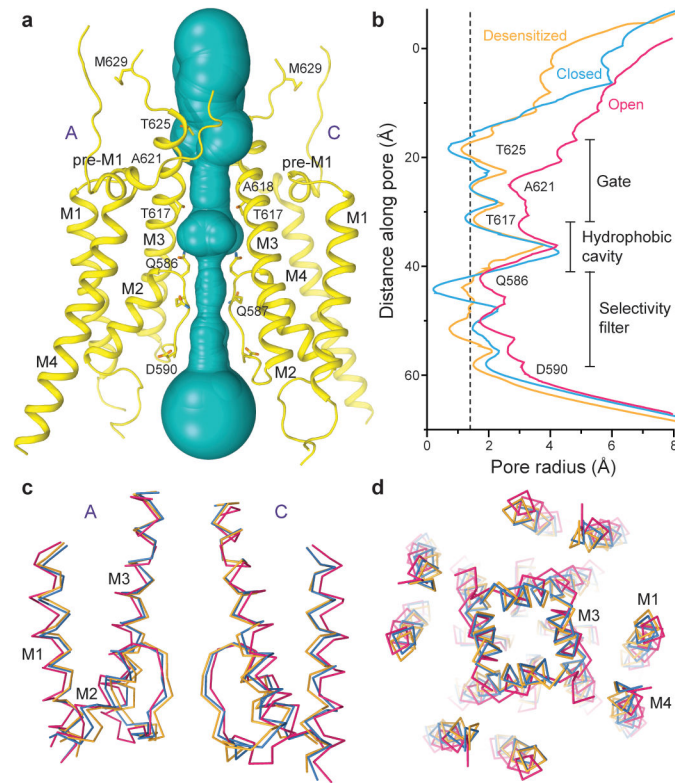
Figure 4. Ion channel pore in open, closed and desensitized states

a, The GluA2-STZ$_{Glu+CTZ}$ ion conduction pathway (cyan) with pore-lining residues in M2 and M3 segments of subunits A and C shown as sticks. **b**, Pore radius calculated using HOLE for GluA2-STZ$_{Glu+CTZ}$ in the open state (pink), GluA2-GSG1L$_{ZK-1}$ in the closed state (blue) and GluA2-2xGSG1L$_{Quis}$ in the desensitized state (orange). **c–d**, TMD ribbon diagrams for the structures in (**b**) viewed parallel to membrane (**c**) or extracellularly (**d**). In (**c**), subunits B and D as well as M4 segments are removed for clarity.
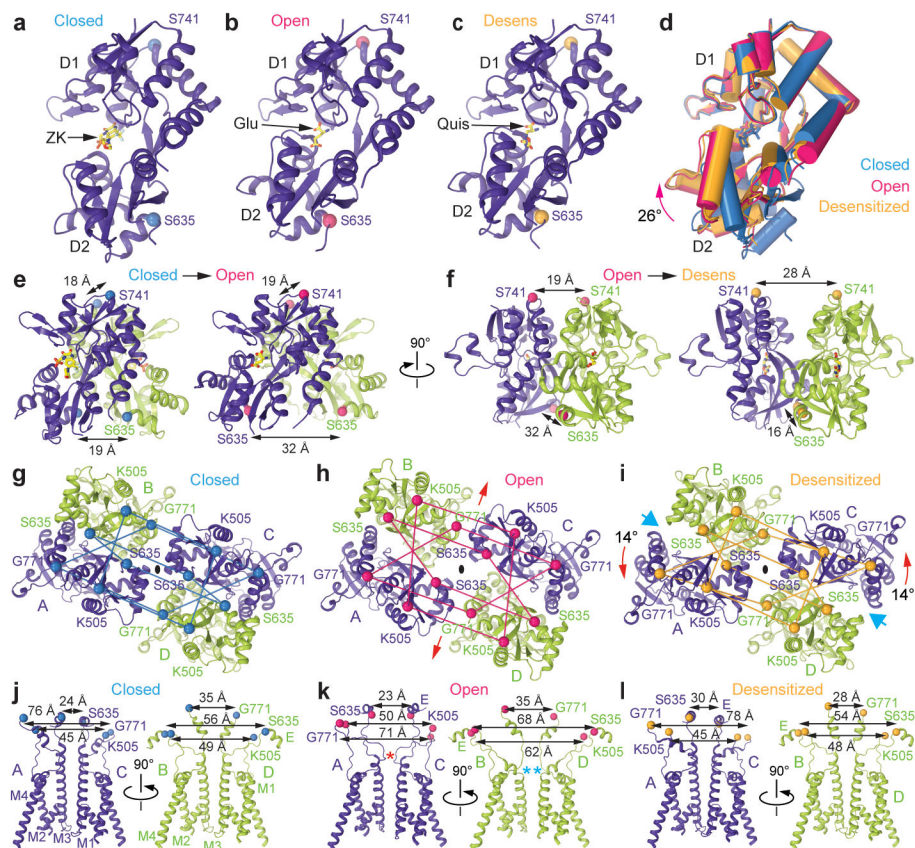
Figure 5. Structural rearrangements in during gating

GluA2 domains are shown for structures of GluA2-GSG1L$_{ZK-1}$ in the closed state (blue), GluA2-STZ$_{Glu+CTZ}$ in the open state (pink) and GluA2-2xGSG1L$_{Quis}$ in the desensitized state (orange). **a–d**, LBD monomers shown individually (**a–c**) or in superposition (**d**). ZK, Glu and Quis molecules are shown in sticks. **e–f**, Changes in LBD dimer conformation upon transition from closed to open (**e**) and open to desensitized (**f**) states. Separation of upper D1 and lower D2 lobes is indicated by arrows. (**g–i**) LBD tetramers viewed from the ion channel. Broadening of the LBD layer in the open state and rotation of the A and C monomers in the desensitized state are indicated by red arrows. Blue arrows in (**i**) point to the cleft between the desensitized state LBD protomers signifying the loss of local LBD dimer 2-fold symmetry and 3-fold reduction of intradimer interface[16]. (**j–l**) S1-M1, M3-S2 and S2-M4 linkers viewed parallel to membrane. The A/C and B/D subunit pairs are shown separately and viewed orthogonally. Distances between Cα atoms of K505, S635 and G771 are indicated. Red and blue stars in (**k**) indicate the S2-M4 linkers extended towards the pore and one helical turn-unwound M3 helices in A/C subunits and kinked M3 helices in the B/D subunits of the open state, respectively.